

CHANDRA OBSERVATIONS OF ABELL 85: MERGER OF THE SOUTH SUBCLUSTER

JOSHUA C. KEMPNER AND CRAIG L. SARAZIN

Department of Astronomy, University of Virginia, P. O. Box 3818, Charlottesville, VA 22903-0818
 jck7k@virginia.edu, cls7i@virginia.edu

AND

PAUL M. RICKER

Department of Astronomy & Astrophysics, University of Chicago, 5640 S. Ellis Ave., Chicago, IL 60637
 ricker@flash.uchicago.edu

Accepted for publication in the Astrophysical Journal.

ABSTRACT

We present an analysis of a highly asymmetric cluster merger from a *Chandra* observation of Abell 85. The merger shows significant disruption of the less massive subcluster from ram pressure effects. Nevertheless, a cold core, coincident with the cD galaxy, is observed to persist in the subcluster. We derive dynamical information from the motion of the cold core through the main cluster's ICM. Multiple derivations of the velocity of the core suggest a Mach number of $\mathcal{M} \approx 1.4$, or $v \sim 2150 \text{ km s}^{-1}$, though with substantial uncertainty. We construct a consistent kinematic model for the merger based on this dynamical analysis. As has been found for other such “cold fronts,” conduction appears to be suppressed across the front. Thermal conduction may be suppressed by a magnetic field with a significant component perpendicular to the subcluster’s direction of motion. The effect of the merger interaction in creating and shaping the observed radio sources is also discussed. It appears most likely that the radio source is due to distorted and detached lobes from the subcluster cD galaxy, rather than being a radio halo.

Subject headings: cooling flows — galaxies: clusters: individual (Abell 85) — intergalactic medium — magnetic fields — shock waves — X-rays: galaxies: clusters

1. INTRODUCTION

Mergers of clusters of galaxies are highly energetic events, releasing a total kinetic energy of $\sim 10^{63}$ ergs into the intracluster medium (ICM). When clusters merge, shocks are driven into the ICM, dissipating the kinetic energy of the merger and heating the gas. These shocks also have nonthermal effects, including the generation of turbulence in the ICM and acceleration of charged particles to relativistic, or cosmic ray, energies. Observations with *Chandra* of merging clusters have provided new insights into the cluster merger process, including the unpredicted discovery of the persistence of cold cores from pre-merger cooling flows well into the lifetime of a merger (“cold fronts;” Markevitch et al. 2000; Vikhlinin et al. 2001b).

Abell 85 is in the early stages of merging with two sub-clusters, each much less massive than the main cluster. One subcluster is merging from the southwest while the other subcluster is merging from the south. The south subcluster will be the focus of our discussion here, while the other subcluster and its associated radio relic will be discussed in a later paper. Abell 85 is unusual in being one of the few clusters known to be in the process of a merger while maintaining a moderate ($107 M_{\odot} \text{ yr}^{-1}$; Peres et al. 1998) cooling flow. Presumably, this implies that the merging subclusters have not yet penetrated the inner few hundred kiloparsecs of the cluster and have therefore not yet been able to disrupt the cooling flow.

The south subcluster is more massive than the southwest subcluster. There has been some uncertainty in the past as to whether or not this subcluster is in fact merging

with the main cluster or is merely seen against the main cluster in projection. Using data from *ASCA*, Markevitch et al. (1998) determined that the temperature in the region of the subcluster is the same as or slightly greater than that of the rest of the main cluster at the same radius. If the subcluster were not merging and were only seen in projection, its smaller mass would give it a lower temperature than that of the main cluster. Thus, the higher temperature indicates that the subcluster is almost certainly interacting.

The redshifts of the galaxies in the southern subcluster are slightly larger than those of the main cluster (Beers et al. 1991; Durret et al. 1998). This suggests that the southern subcluster is either a background cluster or that it is slightly in front of the main cluster and its excess redshift comes from its peculiar motion as it falls into the main cluster. Based on the analysis of Markevitch et al. (1998) and the observations presented in the present paper, we believe that it is merging with the main cluster. Thus, we will assume that the southern subcluster is at essentially the same distance as the main cluster, and that any difference in their observed redshifts is caused by their relative motion along the line of sight as they merge.

The *Chandra* observation and basic data reduction are discussed in § 2. The X-ray image is presented in § 3.1. In § 3.2, we analyze the spectra of interesting regions associated with the southern subcluster. The profiles of the X-ray surface brightness and temperature within the subcluster and in the region ahead of the subcluster are extracted in § 3.3. We discuss the evidence for a merger and X-ray determinations of the merger Mach number in § 4. The pressure increase at the cold front and proper-

ties of the bow shock are used to derive the merger velocity in § 4.1 and 4.2. We construct a consistent kinematic model for the merger in § 5. The suppression of conduction across the cold front is discussed briefly in § 6. There have been claims of a possible radio relic in this cluster as well (Bagchi et al. 1998), which we discuss in § 7. Our results are summarized in § 8. We assume $H_0 = 50 \text{ km s}^{-1} \text{ Mpc}^{-1}$ and $q_0 = 0.5$ throughout this paper. At the cluster redshift of $z = 0.0538$, $1''$ corresponds to 1.43 kpc. All of the errors quoted are at the 90% confidence level.

2. OBSERVATION AND DATA REDUCTION

Abell 85 was observed with ACIS-I detector on *Chandra* in a single 39 ksec observation. Using the count rate in the S3 chip, we excluded data during two small background flares using the *lc_clean*¹ routine written by Maxim Markevitch. This left 36,587 s of useful exposure time. Although the observation included the four ACIS-I chips and the S3 and S4 chips, the analysis presented here will be based on the ACIS-I data only. The focal plane temperature during the observation was -120 C . A raw image of the entire ACIS-I detector in the spectral band 0.3–10 keV is presented in Figure 1.

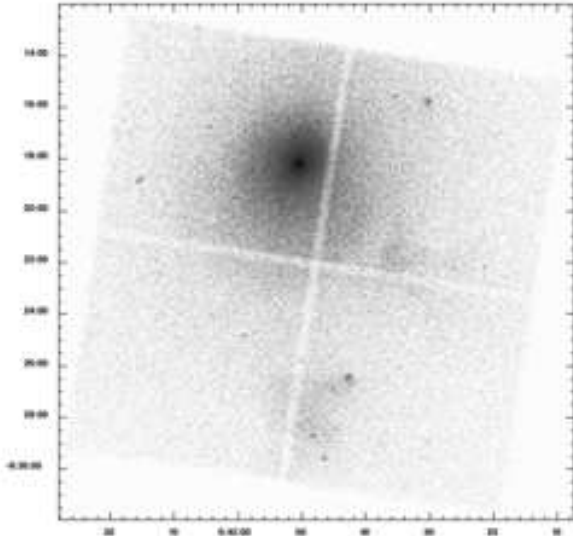


FIG. 1.— Raw X-ray image of Abell 85 in the 0.3–10 keV band, uncorrected for background or exposure. All four ACIS-I chips are shown; the regions of reduced exposure are the interchip gaps. The center of the main cluster and cooling flow are located on the upper left chip, the center of the southwest subcluster is located just above the lower edge of the upper right chip, and the south subcluster is near the bottom and overlaps the two lower chips.

The ACIS-I suffers from enhanced charge transfer inefficiency (CTI) caused by radiation damage early in the mission. We corrected for the quantum efficiency non-uniformity and gain variations caused by this damage, but the degradation in spectral response was not corrected for due to the lack of availability of appropriate response matrices. We used version 1 of the January 29, 2001 gain file and response files. Because of uncertainties in the spectral response at low energy, we limit our spectral analyses to the range 0.7–10.0 keV, excluding the 1.8–2.2 keV band around the mirror iridium edge. We constructed blank sky backgrounds from the March 23, 2001 versions

of Maxim Markevitch’s ACIS-I background photon lists using the routine *make_acisbg*¹.

3. X-RAY PROPERTIES OF THE SOUTHERN SUBCLUSTER

3.1. X-ray Image

Figure 2 shows an adaptively smoothed image of an approximately $6.4'' \times 6.4''$ region around the southern subcluster. The image was smoothed to a signal-to-noise ratio of three for each smoothing beam. The same set of smoothing kernels were used to smooth the blank-sky background image and the exposure map. The smoothed background image was subtracted from the smoothed subcluster image, and the result was divided by the smoothed exposure map.

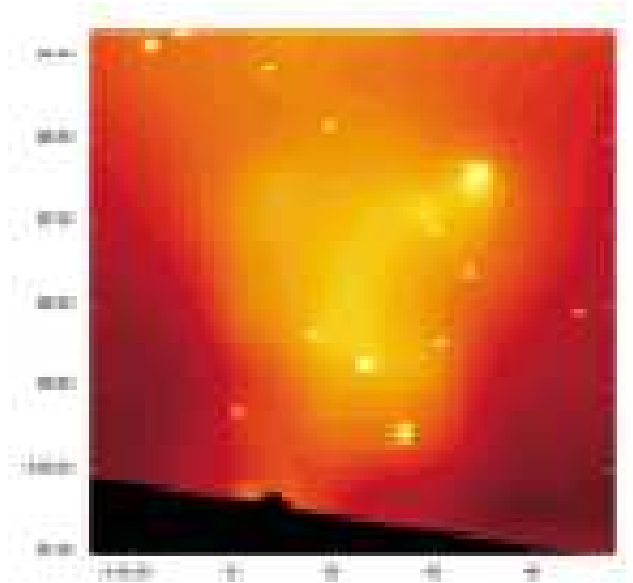


FIG. 2.— Adaptively smoothed image of the south subcluster, corrected for background and exposure. The cold core is at the NW corner of the subcluster.

The subcluster is roughly cone-shaped (Figure 2), with a high surface brightness knot at the northwest corner. This bright region is spatially extended, with a diameter of about $26''$, and is centered on the cD galaxy which is the brightest galaxy in the southern subcluster (see Figure 6 below). The northern edge of this knot shows an abrupt surface brightness edge. This suggests that it is either a merger shock or a “cold front,” the leading edge of a cold core. There is a curved tail of brighter X-ray emission extending to the southeast of the bright knot.

The overall geometry indicates that the ICM in the subcluster has been affected by ram pressure from the gas in the main cluster. The morphology suggests that the south subcluster is in the early stages of merging with the main cluster, and that it is falling into the main cluster for the first time from the south. The sharp edge at the top of the bright knot is symmetrical about a position angle of -15° (15° west of north). The bulk of the subcluster forms a conic distribution centered about a position angle of 123° (58° east of south). This difference between 123° and $165^\circ = (180^\circ - 15^\circ)$ may indicate that the cD galaxy

¹ see <http://hea-www.harvard.edu/~maxim/axaf/acisbg/>

TABLE 1
SPECTRAL FIT PARAMETERS

Region	model	$k_B T$ (keV)	Z (Z_\odot)	χ^2	<i>d.o.f.</i>	net counts
cold core	mekal	$2.3^{+0.6}_{-0.4}$	$0.48^{+0.97}_{-0.27}$	16.7	16	416
cold core	mekal + main cluster	$2.1^{+0.5}_{-0.4}$	$0.53^{+0.65}_{-0.34}$	15.9	16	416
subcluster – cold core	mekal	$6.3^{+0.6}_{-0.5}$	$0.34^{+0.15}_{-0.15}$	254.0	196	8486
subcluster – cold core	mekal + main cluster	$5.5^{+0.7}_{-0.6}$	$0.36^{+0.20}_{-0.19}$	254.6	196	8486
main cluster	mekal	$9.0^{+2.4}_{-1.7}$	$0.52^{+0.67}_{-0.50}$	186.8	168	4527

is moving relative to the center of mass of the subcluster, or that the shape has been affected by the density structure in the subcluster and main cluster gas. In any case, it appears that the transverse component of the velocity of the subcluster relative to the main cluster lies at a position angle between -60° and -10° . The position angle of the center of the main cluster from the subcluster is about $+13^\circ$. This implies that this is an offset merger; the collision is occurring with a nonzero impact parameter and angular momentum.

Several point X-ray sources are also seen in the region of the subcluster (Figure 2). Only two of these have an optical counterpart: the source at R.A. = $00^{\text{h}}41^{\text{m}}50\text{s}.4$, Dec. = $-9^\circ25'48''$ is coincident with the nucleus of the galaxy PGC 93226, which is a cluster member and a radio source (radio source B in Figure 6 below); and the source at R.A. = $00^{\text{h}}41^{\text{m}}59\text{s}.0$, Dec. = $-9^\circ24'49''$ is coincident with a very faint galaxy of unknown redshift (source 1-2117; Slezak et al. 1998).

3.2. X-ray Spectra

We extracted the X-ray spectra of the bright knot coincident with the cD galaxy at the top of the subcluster (“cold core”), of the remainder of the subcluster, and of the main cluster gas at a similar projected distance from the center of the main cluster. The spectrum of the bright knot was extracted from the elliptical region at the center in Figure 3a. The spectrum from the remainder of the subcluster was extracted from a polygonal region encompassing most of the rest of the subcluster, minus the point sources within that region. The main cluster spectrum came from an annular pie wedge to the east of the subcluster and which encompassed the same radii from the cluster center as the subcluster. The spectral fits in these regions are presented in Table 1. The spectra were grouped to have a minimum of 20 counts per channel. As described in § 2, we restricted our spectral analysis to the range 0.7–10.0 keV, minus the band from 1.8–2.2 keV. In the fit to the spectrum of the main cluster, we cut the spectrum off at 9.0 keV because the spectrum of this diffuse emission is dominated by background above this energy. The spectra were fit within *xspec* using the *mekal* model for the thermal emission. The absorption column was fixed at the Galactic value of $2.85 \times 10^{20} \text{ cm}^{-2}$ (Dickey & Lockman 1990). Since the observed emission from the cold core and subcluster presumably contain emission from the main cluster seen in projection in front of and behind these regions, we also fit the spectrum of the cold core and subcluster with two *mekal* thermal components, with the shape of the hotter component fixed at the values found for the main cluster,

and the normalization determined by the relative areas of the regions.

We find that the temperature of the bright knot at the top of the subcluster ($2.1^{+0.5}_{-0.4}$ keV) is much lower than the temperature of the remainder of the subcluster or of the surrounding gas from the main cluster. This shows that this X-ray bright and dense region is a cooling core associated with the central region and central cD galaxy in the subcluster. The sharp surface brightness discontinuity at the northern edge of this knot must be a cold front, rather than a merger shock, since the compressed gas has a lower temperature and specific entropy than the less dense gas (Markevitch et al. 2000; Vikhlinin et al. 2001b).

We also fit the cold core with a cooling flow model, with and without an additional foreground and background contribution from the main cluster. In both cases, the gas was allowed to cool to the minimum allowable temperature, essentially zero. For the fit without the additional component for the main cluster, we fixed the maximum temperature and abundance to those from the third fit in Table 1. We found a cooling rate of $7.3^{+0.7}_{-0.8} M_\odot \text{ yr}^{-1}$. With an additional *mekal* model component set to the main cluster parameters, and with the maximum temperature and abundance set to the parameters from fit number 4 in Table 1, we derived a cooling rate of $6.8 \pm 0.6 M_\odot \text{ yr}^{-1}$. Both fits are consistent with a low present cooling rate. Both fits also had a significantly worse reduced χ^2 than did either of the first two models presented in Table 1.

We fit a single temperature model to the spectrum of the subcluster minus the cold core and found a temperature of $6.3^{+0.6}_{-0.5}$ keV. If we add a model component for the emission from the main cluster, we find a subcluster temperature of $5.5^{+0.7}_{-0.6}$ keV. The former temperature is slightly lower than the value given by Markevitch et al. (1998), but is consistent to within the errors. Our extraction region is smaller than that used by Markevitch et al. (1998) due to the much poorer angular resolution of *ASCA*. Thus, the *ASCA* spectrum may have included more emission from the main cluster, which is hotter. In any case, the bulk of the subcluster is hotter than might be expected for a cluster of this mass and X-ray luminosity, which may indicate that the much of the subcluster gas has been heated by shocks or adiabatic compression associated with the merger.

3.3. Temperature and X-ray Surface Brightness Profiles

We measured the temperature and surface brightness gradients inside the subcluster and in front of the cold front (Figure 3). The temperature measurements in front of the

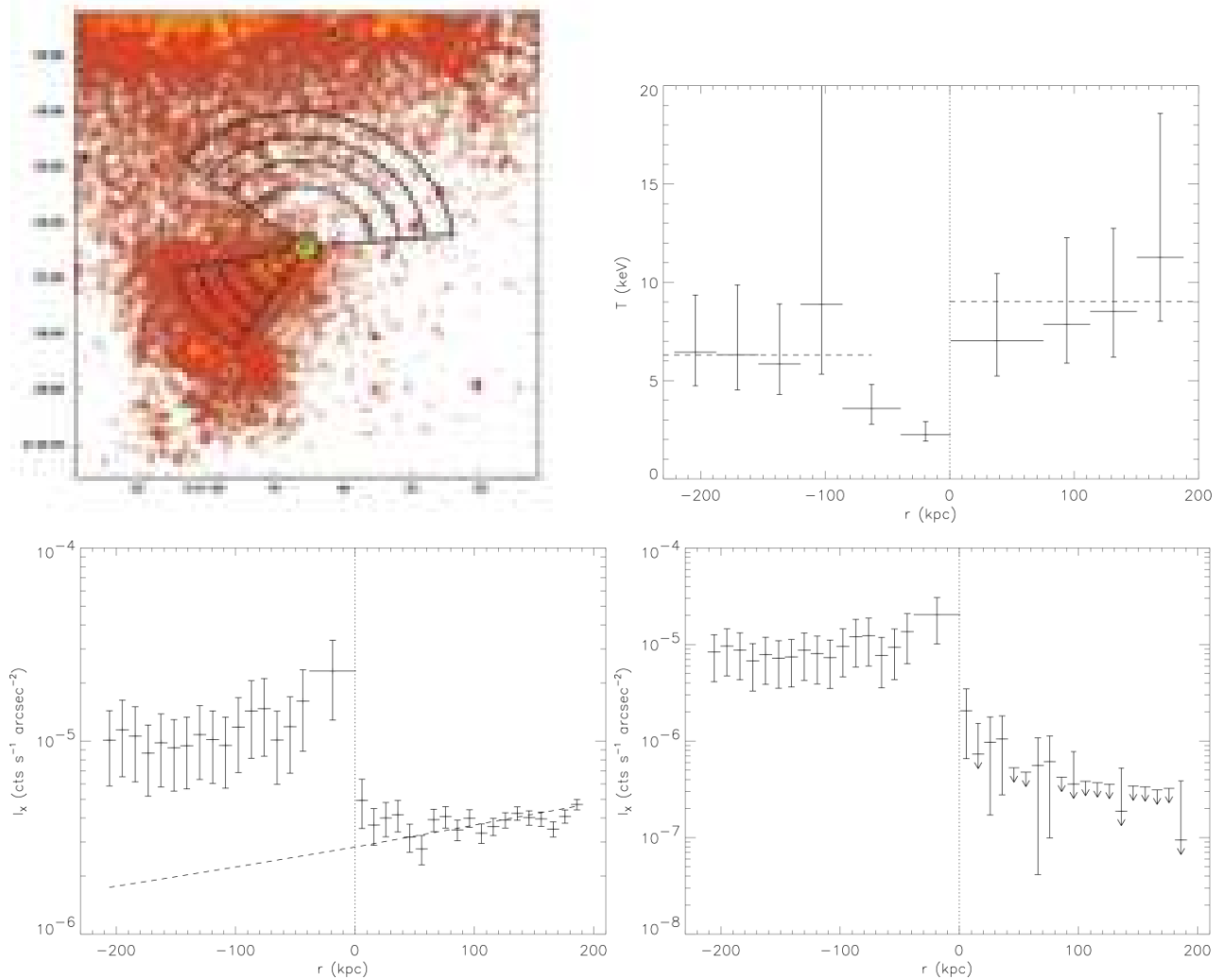


FIG. 3.— (a) Elliptical annular wedge regions used for determining temperatures are shown superposed on a gaussian smoothed image of the south subcluster. (b) Temperature profile in the regions shown in (a). The dotted line indicates the position of the cold front, with positive radii in the direction of motion of the subcluster (i.e., ahead of the cold front). The dashed lines indicate the temperatures from the single-temperature fits given in Table 1. The fit to the subcluster is shown for the radii over which it was determined. (c) X-ray surface brightness from 0.3-10 keV in a set of elliptical annular wedges with the same shape and orientation as those in (a), but more closely spaced. (d) X-ray surface brightness values from (c), after correction for the foreground and background emission from the main cluster. The dashed curve in (c) is the projected surface brightness contribution from the main cluster, which is used to correct the values in (d).

cold front were made by extracting spectra in a wedge of elliptical annuli whose curvature matched that of the cold front. The measurements within the subcluster were made from spectra also accumulated from annular wedges using ellipses self-similar to those in front of the cold front. The size and orientation of the wedges inside the subcluster were determined by the edges of the subcluster, and therefore were not oriented 180° from the wedge in front of the subcluster. While the annular wedges in front of the subcluster were centered along a line 15° west of north, the wedges inside the subcluster were centered on a line $\sim 58^\circ$ east of south. The regions used to extract the spectra are shown in Figure 3a.

We fit single-temperature models to these spectra, with the absorption column set to the Galactic value. The resulting temperatures from fits to these spectra are shown in Figure 3b. The gas in front of the cool core is hot, and

the temperatures are consistent (within the large errors) with the temperature in the main cluster at this radius. The temperature in the cool core of the subcluster is quite low. Behind the cool core, the temperatures in the subcluster rise up to moderately high values.

X-ray surface brightness measurements were made in elliptical annular wedges with the same shape as those used to extract the spectra, but with smaller widths. The resulting surface brightness profile in the 0.3-10 keV band is shown in Figure 3c. As is clear from the image (Figure 2), the highest surface brightness is associated with the cool core. There is a very sharp surface brightness discontinuity (a factor $\gtrsim 5$) at the northern edge of the cool core. The combination of the surface brightness discontinuity with the low temperature in the bright region shows that this is a cold front. The subcluster south of the cool core is much brighter than the gas ahead of the cold front.

If one assumes that the subcluster is merging for the first time, that the motion is transonic, and that the mass of the subcluster is much smaller than that of the main cluster, one would expect the gas far ahead of the cold front would be undisturbed main cluster ICM. Also, main cluster emission may be projected in the foreground and background of the subcluster. To determine the contribution of undisturbed main cluster emission, we measured the surface brightness profile of the main cluster in a wedge to the southeast; this region is essentially the same region as that occupied by the subcluster, but reflected across the north-south axis of symmetry of the main cluster. We fit a β -model to the surface brightness at projected radii from 380 to 680 arcsec, which covers the range of radii containing the subcluster.

The main cluster surface brightness determined from this fit is shown as a dashed curve in Figure 3c. More than ~ 40 kpc ahead of the cold front, the X-ray surface brightness is consistent with the undisturbed main cluster emission within the errors. However, there is some evidence for a rise in the surface brightness just ahead of the cold front; the four values at ~ 0 –40 kpc are all slightly higher than expected. This may indicate that the main cluster gas is compressed ahead of the subcluster and cold front, by a bow shock and/or by adiabatic compression.

To show more clearly the excess X-ray emission associated with the subcluster and any compression of main cluster gas ahead of the cold front, in Figure 3d we subtract the fit to the undisturbed main cluster emission from the surface brightness values in Figure 3c. In most of the region in front of the subcluster, there are only upper limits on the excess emission. There may be some excess emission just ahead of the cold front, but in the residual surface brightness profile only the point from ~ 1 –10 kpc appears to be significantly increased. In the residual profile, the surface brightness of the subcluster is relatively uniform except for the brighter cool core. Thus, the apparent fall-off in the surface brightness of the subcluster with increasing distance from the cold front in Figure 3c may actually be due to projected main cluster emission.

We determined the gas densities in the regions around the cold front and subcluster by deprojection. We assumed different geometries for the subcluster and for the gas ahead of the cold front. For the densities inside the subcluster, we assumed the subcluster to be a cone opening up behind the cold front, with an opening angle determined from the image. We further assumed that this cone's axis of symmetry lies in the plane of the sky. We determined the gas density well ahead of the cold front from the β -model fit to the surface brightness of the main cluster discussed above. We also assumed a spherically symmetric main cluster to do the deprojection. We used the deprojected gas densities and the temperatures from spectral fits to determine the pressures across the cold front.

4. HYDRODYNAMICAL ANALYSIS OF MERGER

We now use the gas temperatures, densities, and pressures derived in § 3.3 to analyze the kinematics and hydrodynamics of the subcluster merger. Our treatment closely follows that in Vikhlinin et al. (2001b). A schematic view of the geometry of the flow of main cluster gas near the cold front is shown in Figure 4), which is adapted from

Vikhlinin et al. (2001b). A bow shock will be present ahead of the cold front if the merger velocity of the cold front relative to undisturbed main cluster gas is supersonic. (There is also a shock in the cold front, but the shocked region will be very narrow if the cool core is much denser than the main cluster gas.) If the motion is subsonic, the flow around the cold front is continuous. For any blunt cold front, there will be a point in front of the cold front where the velocity of the main cluster gas is zero. This stagnation point is labeled “st” in Figure 4).

4.1. Stagnation Pressure at Cold Front

The ratio of the pressures in the main cluster gas far ahead of the cold front to that at the stagnation point, combined with temperature measurements of the gas, can be used to determine the velocity of the cold front (Vikhlinin et al. 2001b). Ideally, we would measure the pressure at the stagnation point in the hot gas. However, since the surface brightness of the hot gas at the stagnation point is actually quite low, we instead measure the pressure in the cool core just behind the stagnation point where the surface brightness is much higher. Because the cold front is a contact discontinuity and the gas is moving subsonically near the stagnation point, the pressure across the cold front is expected to be continuous. The pressure difference between the stagnation point and a point far upstream (region 1 in Figure 4) must be caused by compression of the gas in region 2 by a bow shock and/or adiabatic compression.

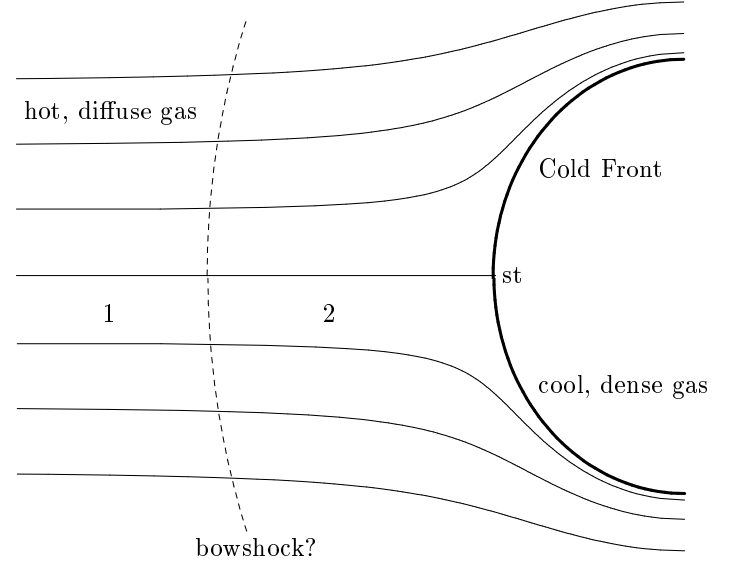


FIG. 4.— Schematic diagram of the flow of hot main cluster gas around a blunt cold front. A bow shock will be present ahead of the cold front if the merger is supersonic. The stagnation point is labeled “st”. Region 1 is unshocked gas of the main cluster; region 2 is gas which has passed through the bow shock (if present).

The ratio of the pressure at the stagnation point to the pressure in the far upstream region 1 is given by (e.g. Landau & Lifshitz 1959, §114)

$$\frac{P_{st}}{P_1} = \begin{cases} (1 + \frac{\gamma-1}{2} \mathcal{M}^2)^{\frac{\gamma}{\gamma-1}}, & \mathcal{M} \leq 1, \\ \mathcal{M}^2 (\frac{\gamma+1}{2})^{\frac{\gamma+1}{\gamma-1}} (\gamma - \frac{\gamma-1}{2\mathcal{M}^2})^{-\frac{1}{\gamma-1}}, & \mathcal{M} > 1. \end{cases} \quad (1)$$

Here P_{st} and P_1 are the pressures at the stagnation point and in region 1, respectively and $\gamma = 5/3$ is the adiabatic index for a fully ionized plasma. $\mathcal{M} \equiv v_1/c_{s1}$ is the Mach number of the cold core, v_1 is the cold core's velocity relative to the upstream gas, and c_{s1} is the sound speed in that gas.

We do indeed measure a higher pressure inside the cold core as compared to the undisturbed gas in front of the core. The best fit measurement is $P_{st}/P_1 = 3.4$ which implies a Mach number of 1.4. This measurement assumes that the separation between the main cluster and the subcluster is equal to their projected separation, so P_1 is measured at the projected radius of the subcluster within the main cluster. The formal errors yield a wide range in allowable Mach numbers, from 0 to 3.3, but since not all the sources of error are independent, the actual error is probably somewhat smaller. While a Mach number of zero is allowed, the morphology of the system makes such a value highly unlikely. In any case, the best fit value of the pressure ratio requires that the merger motions be slightly supersonic.

4.2. Possible Bow Shock

For a supersonic cold core, a bow shock should also form in front of the cold core. Assuming that the density and temperature of the gas in region 1 is constant, the bow shock should have a predictable “stand-off” distance, d_s , which is the shortest distance from the stagnation point to the bow shock (Vikhlinin et al. 2001b). This distance can be calculated using the approximate method given by Moekel (1949), and depends only on the value of \mathcal{M} and on the shape of the cold front. A useful plot of the stand-off distance versus Mach number is given in Sarazin (2002, Figure 4). For $\mathcal{M} \gtrsim 2$, the stand-off distance of the shock is not very sensitive to the value of \mathcal{M} , while for smaller Mach numbers the distance increases rapidly. For the best fit value of $\mathcal{M} = 1.4$, the expected stand-off distance is $d_s \sim 18$ kpc if we treat the cold front as a spherical surface with a radius of curvature of 19 kpc. Such a bow shock would compress the gas in region 2, and should produce a measurable increase in the X-ray surface brightness, I_X , in that region. A possible surface brightness excess is seen in the ~ 20 kpc immediately upstream from the cold front, but it is significant at only slightly greater than the 1.7σ level. While this surface brightness excess is not visible in the image of the cluster, we might expect such a feature to be more visible in profile given the significant azimuthal averaging done to create the profile.

Given enough source photons, the spatial resolution of *Chandra* would be sufficient to measure the expected stand-off distance of the bow shock, which corresponds to $\sim 5\text{--}15''$. However, the surface brightness in the hot gas ahead of the cold front is too low to allow d_s to be accurately determined from the available data. Thus, all we can conclude is that the expected values of the stand-off distance are consistent with the (marginal) evidence for an increase in the X-ray surface brightness within ~ 20 kpc of the cold front.

We can also use the Rankine-Hugoniot shock jump conditions at the putative bow shock to independently determine the Mach number (e.g. Landau & Lifshitz 1959,

§85). The shock jump conditions yield

$$\frac{1}{C} = \frac{2}{\gamma+1} \frac{1}{\mathcal{M}^2} + \frac{\gamma-1}{\gamma+1}, \quad (2)$$

where $C \equiv \rho_2/\rho_1$ is the shock compression. Because we do not have spectra or temperatures determined on the scale of the bow shock, we estimate the shock compression from the small increase in the surface brightness as $C \approx (I_{X2}/I_{X1})^{1/2}$. The observed surface brightness increase in the first 10 kpc is a factor of ~ 1.7 , which implies that $C \sim 1.3$. This implies $\mathcal{M} \sim 1.2$. It is likely that the finite resolution with which the surface brightness contrast was determined and projection effects cause the shock compression to be underestimated. Thus, this value for the Mach number is consistent with that determined from the pressure increase at the stagnation point. If we assume the Mach number determined by the stagnation condition $\mathcal{M} \sim 1.4$, the expected shock compression is $C \sim 1.6$. Projection effects (if the cluster is not moving in the plane of the sky) would cause us to overestimate the stand-off distance and underestimate the Mach number. Projection could also cause us to inaccurately determine the true shape of the cold front.

5. MERGER KINEMATICS

Since it provides a consistent fit to the stagnation pressure, the bow shock compression, and the bow shock stand-off distance, we will adopt the merger Mach number of $\mathcal{M} \approx 1.4$. The sound speed in the upstream gas is $\approx 1540 \text{ km s}^{-1}$, so a Mach number of 1.4 implies a merger velocity of $v \approx 2150 \text{ km s}^{-1}$.

5.1. Kinematic Model

We now construct a kinematic model for the merger which is consistent with the X-ray and optical observations of the main cluster and subcluster. Because the errors on our determination of the Mach number are large, the parameters of this model are not well constrained. We therefore do not suggest that this model is the only possible interpretation of the data, but that it is merely a “toy model” that is adequate to explain the data given the best-fit values from the various hydrodynamic tests. The model, then, is presented as illustrative rather than interpretive, using the best-fit parameters from the hydrodynamic analyses as the primary constraints of the model. We also discuss the implications of this model for the merger.

The parameters of the model are shown in Figure 5. We will approximate the subcluster as a point mass with a single velocity relative to the main cluster. We will also assume that the mass of the subcluster is small relative to that of the main cluster, so we can treat the subcluster as a test particle falling into the extended mass distribution of the main cluster. We put the center of the main cluster at the center of our coordinate grid, and using polar coordinates, we define the x -axis to be parallel to North and the z -axis to be the line of sight, with the positive z -axis extending away from the observer. Let the vector \vec{d} be the position of the subcluster relative to the main cluster (direction from the main cluster to the subcluster). The components of \vec{d} are defined by its magnitude d , the angle to the line of sight θ_d (from the positive z -axis), and the

position angle on the plane of the sky ϕ_d measured counterclockwise from the north. Similarly, let \vec{v} be the velocity of the subcluster relative to the main cluster, with magnitude v , and direction given by the angles θ_v and ϕ_v . We also define ψ to be 180° minus the angle between \vec{d} and \vec{v} .

On the X-ray image (Figure 1), the subcluster center is located at a position angle of $\phi_d = 194^\circ$ from the main cluster. The position angle of the direction of motion, ϕ_v is less certain, since the curvature of the cold front suggests $\phi_v \sim -15^\circ$ whereas the body of the subcluster is more consistent with $\phi_v \sim -58^\circ$. We will adopt the average value of $\phi_v \approx -36^\circ$.

We can estimate the radial component of the relative velocity of the subcluster from the optical redshifts of the main cluster and subcluster. We will adopt the velocity of the subcluster cD galaxy as representative of the subcluster; in any case, it is most closely related to the cold front, which was used to derive the merger velocity. Beers et al. (1991) give the redshift of the subcluster cD galaxy as $z = 0.05633 \pm 0.00012$, while the galaxies within 5/25 of the center of the cluster have a mean redshift of 0.0538 ± 0.0050 (Durret et al. 1998). Combining the line-of-sight velocity determined from the optical redshifts with the velocity merger velocity determined in § 4 from the X-ray data, we find that the direction of motion of the subcluster relative to the main cluster is between $\theta_v = 63^\circ$ and 76° from the line of sight, or 14° to 27° from the plane of the sky. We adopt the average value of $\theta_v \approx 71^\circ$.

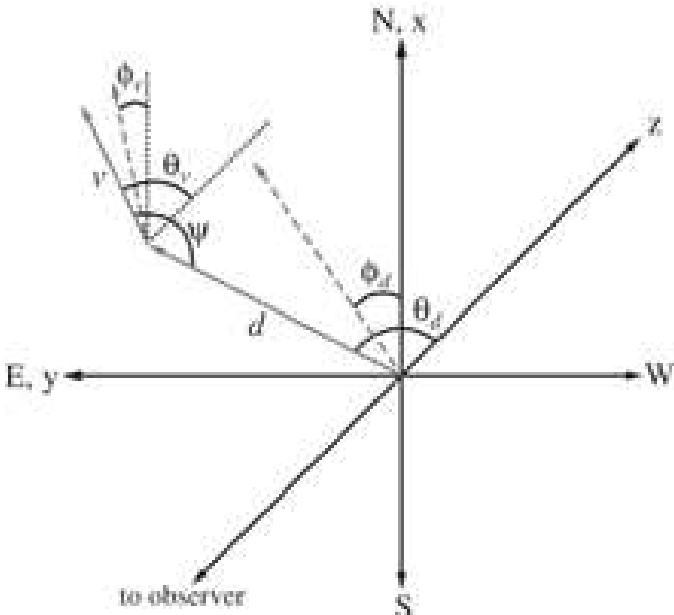


FIG. 5.— Schematic diagram of the kinematic model. The position of the subcluster relative to the main cluster is given by the vector \vec{d} , and \vec{v} is the velocity of the subcluster relative to the center of the main cluster. The z -axis is along the line-of-sight. The dashed lines are projections of the direction and velocity vectors onto the plane of the sky. The dotted line is parallel to the N-axis. The small inset shows the projection of the direction and velocity vectors onto the N - z plane, with the dotted line parallel to the z -axis.

It is difficult to determine the angle between the separation of the main cluster and subcluster, \vec{d} , and the line-of-sight. Initially, we will assume that the main cluster and subcluster are separated in the plane of the sky ($\theta_d = 90^\circ$), so that the separation between the main cluster and clus-

ter is equal to the projected separation, $d = 730$ kpc. The angle between \vec{d} and \vec{v} is then $\psi = 53^\circ$, and the impact parameter of the merger is $b \approx 580$ kpc.

5.2. Infall Velocity

We now compare the merger velocity inferred from the hydrodynamics of the cold front and subcluster with the infall velocity expected for the subcluster and main cluster. Reiprich & Böringer (2002) derive a virial mass for the main cluster of $M_{200} = 1.080 \times 10^{15} M_\odot$ for a virial radius $r_{200} = 2.66$ Mpc. We will assume that the main cluster mass is much larger than that of the south subcluster. We will assume that the subcluster has fallen into the main cluster from its turn-around distance of 5.5 Mpc, which is the value if the age of the Universe is 13 Gyr. As noted above, we initially assume that the main cluster and subcluster are separated in the plane of the sky.

We will consider two models for the mass distribution and potential of the main cluster. We first consider a singular isothermal sphere out to the virial radius, which has a potential given by

$$\Phi(r) = -2\sigma^2 \times \begin{cases} 1 + \ln(r_{200}/r), & r \leq r_{200}, \\ r_{200}/r, & r \geq r_{200}. \end{cases} \quad (3)$$

Here, $\sigma = (GM_{200}/2r_{200})^{1/2} \approx 934$ km s $^{-1}$ is the velocity dispersion. The infall velocity at the subcluster's current projected distance of 730 kpc is 2520 km s $^{-1}$. We also consider a model in which the density within the virial radius is given by the Navarro, Frenk, & White model (1997, hereafter NFW), for which the potential is

$$\Phi(r) = -\frac{GM_{200}}{r_s} \times \begin{cases} \frac{\ln(1+x) - \frac{1}{1+c}}{\ln(1+c) - \frac{c}{1+c}}, & r \leq r_{200}, \\ \frac{1}{x}, & r \geq r_{200}. \end{cases} \quad (4)$$

Here, r_s is the scale radius, and $x \equiv r/r_s$. We adopt a concentration parameter $c \equiv r_{200}/r_s = 10$, which is consistent with NFW's simulations for cluster-mass halos. For this potential, the predicted infall velocity at the projected distance is 2740 km s $^{-1}$.

For either potential, the infall velocity at the projected separation is somewhat larger than the velocity we determined from the X-ray observations of the merger hydrodynamics. Given the large errors in the determinations of the velocities, this difference may not be significant. As first noted by Markevitch et al. (1999), the degree of agreement between the merger velocity determined by hydrodynamical measurements and that expected from infall can be used to test the hypothesis that the intracluster medium is predominantly a non-relativistic, thermal plasma. That is, the calculation of the merger velocity from shock conditions (equation 2) assumes that the merger shock energy is thermalized, and is not converted into relativistic particles, or magnetic fields, or turbulence. All of the hydrodynamic diagnostics require that the intracluster medium act as a $\gamma = 5/3$ gas. Thus, the difference between our hydrodynamical estimate of the merger velocity and the predicted infall velocity (assuming the main cluster and subcluster are separated in the plane of the sky) could suggest that the kinetic energy of the merger is not thermalized particularly efficiently, but instead goes partially into turbulence, magnetic fields, or relativistic particles. As noted by Markevitch et al. (1999), this argument is somewhat circular, as the mass of the cluster was also determined from

hydrostatic equilibrium assuming purely thermal pressure support. Given the uncertainties in the determination of merger velocity and infall velocity, we will instead take the crude agreement between the two speeds as an indication that at least a significant fraction of the merger energy ($\gtrsim 50\%$) is thermalized.

Our initial estimate of the infall velocity was based on the assumption that the main cluster and the subcluster were separated in the plane of the sky ($\theta_d = 90^\circ$). If this is not true, the actual separation d will be larger than the projected separation of 730 kpc, and the predicted infall velocity will be lowered. To illustrate this effect, we construct a consistent model for the merger geometry and kinematics in which the merger velocity equals the predicted infall velocity. As we move the subcluster further out in the main cluster potential, the density and hence the pressure in the ambient medium drops, thereby increasing the pressure ratio used to determine the Mach number. This in turn increases the Mach number we would measure, lessening the need to place the subcluster significantly in front of or behind the main cluster.

Given the large errors in the two numbers, our model is certainly not a unique solution, but is consistent with the current best-fit values of the parameters. For the isothermal potential (equation 3), this consistent solution requires that $d \approx 820$ kpc, while for the NFW potential (equation 4) we find $d \approx 860$ kpc. The Mach numbers we derive are $\mathcal{M} = 1.6$ for the isothermal potential and $\mathcal{M} = 1.7$ for the NFW potential. The corresponding velocities are $v \approx 2460 \text{ km s}^{-1}$ and $v \approx 2610 \text{ km s}^{-1}$ respectively. For both solutions, we assume that the sound speed does not vary over the range of radii in question. If we were to allow the sound speed to vary, it would decrease slightly at larger radii, increasing the physical separation that we determine. To be specific, we will adopt the isothermal result. This distance implies that the angle between the separation and the line of sight is either $\theta_d \approx 64^\circ$ or $\theta_d \approx 116^\circ$. The former value implies that the $\psi \approx 66^\circ$, which means that the subcluster is moving nearly perpendicular to the radius from the center of the main cluster, and about to start exiting the cluster. The observed morphology of the X-ray image of the subcluster seems inconsistent with this interpretation. Thus, we adopt the solution with $\theta_d \approx 144^\circ$ and $\psi \approx 46^\circ$, in which the subcluster is moving into the main cluster, probably for the first time. In summary, our consistent kinematic model has $v \approx 2460 \text{ km s}^{-1}$, $\theta_v \approx 71^\circ$, $\phi_v \approx -36^\circ$, $d \approx 820$ kpc, $\theta_d \approx 116^\circ$, $\phi_d \approx 194^\circ$, and $\psi \approx 46^\circ$. The subcluster is closer to us than the main cluster, and is falling into the main cluster.

5.3. Angular Momentum and Impact Parameter

As noted above in § 3.1, the direction of the merger velocity is not parallel to the separation of the centers of the main cluster and subcluster. The transverse component of the merger velocity lies at an angle of $\sim 50^\circ$ with respect to the projected separation of the two clusters. This implies that this is an offset merger; the collision is occurring with a nonzero impact parameter and angular momentum. If we adopt the consistent model for the merger kinematics which we have just discussed, the angle between the velocity and the separation is $\psi \approx 46^\circ$, and the impact

parameter for the collision is $b = d \sin \psi \approx 750$ kpc. This is 3.7 times the core radius we determine from a β -model fit to the cluster.

A useful dimensionless form for the angular momentum is given by the λ parameter, defined as (Peebles 1969)

$$\lambda \equiv \frac{J|E|^{1/2}}{GM^{5/2}}. \quad (5)$$

Here J is the total angular momentum of the merged cluster, E is its total energy, and M is its mass. We estimated the value of λ implied by the merger velocity and impact parameter of the subcluster by differentiating equation (5), assuming the mass of the subcluster is much smaller than that of the main cluster. We assumed that the orbital angular momentum of the subcluster was parallel to the initial angular momentum of the main cluster, and ignored the initial internal angular momentum of the subcluster. Using the kinematic parameters for our consistent model for the merger, we find $\lambda \approx 0.21$. Fixing v , θ_v , and the projected angles ϕ_d and ϕ_v at the values from the consistent model, and allowing the value of θ_d to vary, we find a minimum value of λ of about 0.16. If the initial spin of the main cluster is not aligned with the orbital angular momentum of the subcluster, the value of λ would be an upper limit. These values are both somewhat larger than the median values of 0.05–0.1 expected from tidal effects in large scale structure. This may reflect the large uncertainties in the kinematic parameters. If this large angular momentum is correct, it might be the result of tidal effects associated with the triple merger occurring in Abell 85 (i.e., the fact that there are two merging subclusters). Alternatively, it may be that mergers with small subcluster have a larger range of values of λ , which average out when many small subclusters merge to form a larger halo.

6. SUPPRESSION OF CONDUCTION ACROSS THE COLD FRONT

As discussed in § 3.1, the cold front is seen as a sharp surface brightness discontinuity, with a dramatic increase in surface brightness in the cold gas over only a few kiloparsecs. From the surface brightness profile in Figure 3, the change in surface brightness occurs over at most 20 kpc—half the width of the elliptical region on the cold core or the width of about 2 bins ahead of the cold front. The raw image suggests that it is actually quite a bit narrower than this, but we are limited by photon statistics to the aforementioned resolution. Unfortunately, the same photon statistics prevent us from measuring the temperature gradient on this size scale. However, because the pressure is continuous on the large scale of our measurements and is presumed to be continuous on the smaller scale of the cold front as well, the observed density gradient should be accompanied by a temperature gradient of the opposite sign and with the same length scale. Therefore, while the width of the gradient is determined from the surface brightness, we can assume that the same width applies to the temperature gradient. Thermal conduction should smear out any such sharp edges to a length a few times the electron mean free path in a relatively short time. However, conduction appears to be suppressed in the case of Abell 85, as it does in other clusters with observed cold fronts (e.g. Abell 2142, Abell 3667; Ettori & Fabian 2000; Vikhlinin et al. 2001b).

Ettori & Fabian (2000) showed that thermal conduction should smear out the temperature gradient to a width δr on a characteristic timescale

$$\delta\tau = \frac{\delta r}{\bar{v}}, \quad (6)$$

where

$$\bar{v} = \frac{2}{3} \frac{\kappa}{n_e k_B T_e} \frac{d(k_B T_e)}{dr} \quad (7)$$

is the characteristic velocity of the diffusion. Here,

$$\kappa = 8.2 \times 10^{20} \left(\frac{k_B T_e}{10 \text{ keV}} \right)^{5/2} \text{ erg s}^{-1} \text{ cm}^{-1} \text{ keV}^{-1} \quad (8)$$

is the thermal conductivity, and n_e and T_e are the electron number density and temperature, respectively. For the upper limit on the width of the cold front of 20 kpc, the diffusion timescale is 2.0×10^6 yr.

At the subcluster's current velocity and distance from the cluster center, the relevant timescale for interaction is roughly $d/v \approx 5.6 \times 10^8$ yr. This means that in order for thermal conduction to have failed to erase the sharp edge of the cold front, conduction must be suppressed by at least a factor of 280–2700. In fact, since the rate of conduction is independent of density, the time over which conduction has had a chance to act is probably somewhat longer, meaning that the degree of suppression is probably even higher.

One mechanism that has been suggested for this suppression is the existence of a magnetic field perpendicular to the direction of diffusion, i.e. parallel to the surface of the discontinuity (Vikhlinin et al. 2001b). A tangled magnetic field would serve the same purpose, with a maximum loop size equal to the width of the front.

7. SUBCLUSTER/RADIO SOURCE INTERACTION

The possible existence of a large scale radio halo or relic in the southern subcluster in Abell 85 was raised by Bagchi et al. (1998). As shown in Figure 6, the diffuse emission was later resolved by Giovannini & Feretti (2000) into what may be a tailed source associated with a dead or dying AGN in the dominant galaxy of the subcluster, where the nuclear emission is very faint compared to the radio lobes. If this is in fact its origin, the shape of the tail is well explained by the merger interaction. Figure 6 shows that the source associated with the cD galaxy in the subcluster (Source D) has possible weak nuclear emission, and a lumpy C-shaped extended source to the southeast of the cD galaxy. The radio emission has no significant extent north of the subcluster's leading edge, and the bulk of the radio emission follows the bright X-ray arc through the subcluster. If it is indeed a tailed galaxy, this shape implies that the same ram pressure forces which have shaped the subcluster have also bent the lobes of the AGN into their current shape.

An alternative explanation for the diffuse radio emission is that this is a small, merger-induced halo in the subcluster. The fact that its surface brightness correlates roughly with that of the X-ray gas is consistent with findings for other halos, as is its steep spectral index ($\alpha_{0.3}^{1.4} \sim 2-2.5$; Giovannini & Feretti 2000). On the other hand, the radio source is quite overluminous compared to the expected radio power derived from the empirical relation between

X-ray temperature or luminosity and radio halo power (Liang et al. 2000; Feretti 2000). For the observed X-ray luminosity of the subcluster of 5×10^{43} erg s $^{-1}$ (rest frame 0.1–2.4 keV), the empirical relation would require a monochromatic radio power of only 4×10^{21} W Hz $^{-1}$ at 1400 MHz in the cluster rest frame, compared to the observed value of 1.8×10^{24} W Hz $^{-1}$ (Feretti 2001) Furthermore, halos have previously only been observed in the hottest and most massive clusters, never in a cluster as small and cool as this subcluster. While previous observations may have been biased towards finding halos in hot clusters (Kempner & Sarazin 2001), it would nonetheless be surprising to find a halo in such a cool, low luminosity cluster. Our observations are therefore more consistent with the interpretation of the source being a tailed radio galaxy (Giovannini & Feretti 2000) than with it being a radio halo or relic.

Source “B” in Figure 6 is a narrow angle tail (NAT) source studied in detail by O’Dea & Owen (1985). It has a redshift of $z = 0.0579$ (Wegner et al. 1999), which is within the dispersion of the main cluster. Since the line of sight component of the subcluster’s infall velocity is so small, however, it is not possible to determine whether or not this galaxy is a member of the subcluster or of the main cluster based solely on radial velocity information. The direction of the tail, plus the fact that the radio tail does not appear to be interacting with the flow around the subcluster, suggest that it is seen in projection in front of or behind the subcluster, and that it is a member of the main cluster.

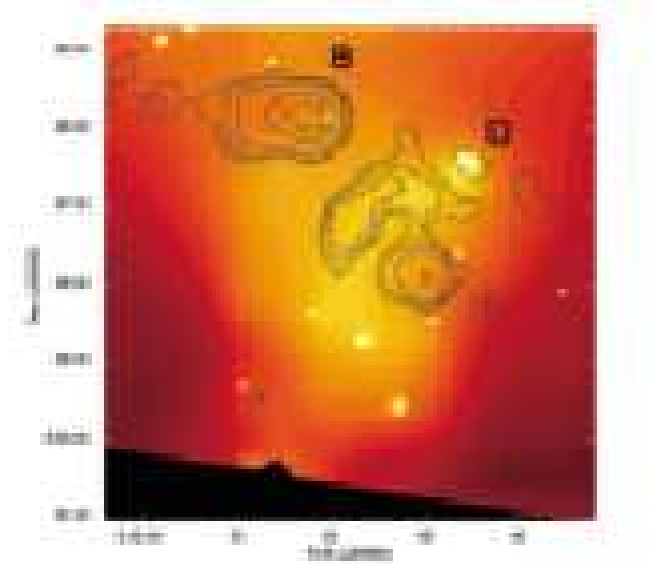


FIG. 6.— Radio contour map at 90 cm of the “B” and “D” sources (from Giovannini & Feretti 2000) in the region of the southern subcluster, overlaid on the adaptively-smoothed *Chandra* image of the subcluster (color, from Figure 2). The D source appears to be associated with the cD galaxy in the south subcluster, while the B source is associated with another cluster galaxy.

8. SUMMARY

Our analysis of the south subcluster in Abell 85 from ~ 37 ksec of *Chandra* data has revealed several interesting features. The most obvious is a confirmation that the subcluster is indeed merging with the the main cluster. The

subcluster contains a remnant cold core which has survived the early stages of the merger. It is smaller and more discrete than similar structures found in other clusters such as Abell 2142 (Markevitch et al. 2000), Abell 3667 (Vikhlinin, Markevitch, & Murray 2001b), and RX J1720.1+2638 (Mazzotta et al. 2001), and is perhaps more akin to the “bullet” in 1E0657-56 (Markevitch et al. 2002) or the “tongue” seen in Abell 133 (Fujita et al. 2002).

Based on the ratio of the pressure at the stagnation point of the cold front to that far upstream, on the stand-off distance of a possible bow shock, and on the shock compression from the bow shock, we find a consistent Mach number and velocity for the merger of $\mathcal{M} \approx 1.4$ and $v \approx 2150 \text{ km s}^{-1}$. By comparing this velocity to the radial velocity of the subcluster relative to that of the main cluster, we have determined that the merger velocity is about 19° from the plane of the sky. We find a consistent kinematic model for the merger in which the subcluster is in front of and falling into the main cluster. This model is consistent with the expected merger velocity if the subcluster and main cluster have fallen towards one another due to gravity from their turn-around distance in the Hubble flow.

The X-ray observations indicate that this is an offset merger with a finite impact parameter and a significant angular momentum. A crude estimate based on our consistent kinematic model suggests an angular momentum

parameter of $\lambda \sim 0.2$, which is somewhat larger than the median values expected due to tidal torques.

Magnetic fields in the cold core may be responsible for suppressing thermal conduction across the cold front. This would explain the sharpness of the front, which should be smeared out by conduction in the absence of a magnetic field. The magnetic fields in the cold core may be high as a result of a cooling flow or the AGN located in the central cD galaxy.

We confirm the assertion that the diffuse radio structure in the subcluster is not a cluster radio halo or relic, but is more likely to be a tailed galaxy with a weak or dead nucleus. We also show that its morphology has been shaped by ram pressure in the merger interaction.

Support for this work was provided by the National Aeronautics and Space Administration, primarily through *Chandra* Award Number GO0-1173X, but also through GO1-2122X, and GO1-2123X, all issued by the *Chandra* X-ray Observatory Center, which is operated by the Smithsonian Astrophysical Observatory for and on behalf of NASA under contract NAS8-39073. We are grateful to Gabriele Giovannini and Luigina Feretti for providing detailed information about and images of the radio sources. We also thank Maxim Markevitch for helpful discussions regarding the kinematic model.

REFERENCES

Bagchi, J., Pislar, V., & Lima Neto, G. B. 1998, MNRAS, 296, L23
 Beers, T. C., Forman, W., Huchra, J. P., Jones, C., & Gebhardt, K. 1991, AJ, 102, 1581
 Dickey, J. M., & Lockman, F. J. 1990, ARA&A, 28, 215
 Durret, F., Felenbok, P., Lobo, C., & Slezak, E. 1998, A&A, 129, 281
 Ettori, S., & Fabian, A. C. 2000, MNRAS, 317, L57
 Feretti, L. 2000, preprint (astro-ph/0006379)
 Feretti, L. 2001, private communication
 Fujita, Y., Sarazin, C. L., Kempner, J. C., Andernach, H., Ehle, M., Roy, A. L., Rudnick, L., & Slee, O. B. 2002, ApJ, in press
 Giovannini, G., & Feretti, L. 2000, New Astronomy, 5, 335
 Kempner, J. C., & Sarazin, C. L. 2001, ApJ, 548, 639
 Landau, L. D., & Lifshitz, E. M. 1959, Fluid Mechanics (London: Pergamon)
 Liang, H., Hunstead, R. W., Birkinshaw, M., & Andreani, P. 2000, ApJ, 544, 686
 Markevitch, M., Forman, W. R., Sarazin, C. L., & Vikhlinin, A. 1998, ApJ, 503, 77
 Markevitch, M., Sarazin, C. L., & Vikhlinin, A. 1999, ApJ, 521, 526
 Markevitch et al. 2000, ApJ, 541, 542
 Markevitch, M., Gonzalez, A. H., David, L., Vikhlinin, A., Murray, S., Forman, W., Jones, C., & Tucker, W. 2002, ApJ, 567, 27
 Mazzotta, P., Markevitch, M., Vikhlinin, A., Forman, W. R., David, L. P., & VanSpeybroeck, L. 2001, ApJ, 555, 205
 Moekel, W. E. 1949, Approximate Method for Predicting Forms and Location of Detached Shock Waves Ahead of Plane or Axially Symmetric Bodies, NACA Technical Note 1921
 Navarro, J. F., Frenk, C. S., & White, S. D. M. 1997, ApJ, 490, 493
 O’Dea, C. P., & Owen, F. N. 1985, AJ, 90, 927
 Peebles, P. J. E. 1969, ApJ, 155, 393
 Peres, C. B., Fabian, A. C., Edge, A. C., Allen, S. W., Johnstone, R. M., & White, D. A. 1998, MNRAS, 298, 416
 Reiprich, T. H., & Böringer, H. 2002, ApJ, 567, 716
 Sarazin, C. L. 2002, in Merging Processes in Clusters of Galaxies, ed. L. Feretti, I. M. Gioia, & G. Giovannini (Dordrecht: Kluwer), in press (astro-ph/0105418)
 Slee, O. B., Roy, A. L., Murgia, M., Andernach, H., & Ehle, M. 2001, AJ, 122, 1172
 Slezak, E., Durret, F., Guibert, J., & Lobo, C. 1998, A&AS, 128, 67
 Vikhlinin, A., Markevitch, M., & Murray, S. M. 2001a, ApJ, 549, L47
 Vikhlinin, A., Markevitch, M., & Murray, S. M. 2001b, ApJ, 551, 160
 Wegner, G., Colless, M., Saglia, R. P., McMahan, R. K. Jr., Davies, R. L., Burstein, D., & Baggley, G. 1999, MNRAS, 305, 259